CrossMark

ORIGINAL ARTICLE

Grindability evaluation and tool wear during grinding of Ti$_2$AlNb intermetallics

Xinxin Xi[1] · Wenfeng Ding[1] · Yucan Fu[1] · Jiuhua Xu[1]

Abstract This article aims at providing a fundamental performance evaluation when grinding Ti$_2$AlNb intermetallics using SiC abrasive. The wheel speed is fixed at 20 m/s while a range of depth of cut (5–20 μm) and workpiece infeed speed (3–12 m/min) are applied. For better understanding, two kinds of common difficult-to-cut materials, i.e., Ti-6Al-4V titanium alloy and Inconel718 nickel-based superalloy are also ground to form a comparison. As for the equal grinding parameters, the normal and tangential grinding forces of Ti$_2$AlNb intermetallics are found to be about twice of those of Ti-6Al-4V alloy, and be only a third and a half of those of Inconel718 alloy, respectively. In addition, Ti$_2$AlNb intermetallics shows more severe tool wear and associated lower G-ratio compared to Inconel718 alloy as a result of strong affinity for SiC abrasives. For the surface integrity, Ti$_2$AlNb intermetallics reveal the same ground surface roughness level, i.e., 0.3–0.6 μm for the applied grinding parameters, with Ti-6Al-4V alloy and Inconel718 alloy. A white layer is easily formed during grinding of Ti$_2$AlNb intermetallics, which adversely affects the machined surface integrity.

Keywords Ti$_2$AlNb intermetallics · Grindability · Tool wear · Surface integrity

✉ Wenfeng Ding
  dingwf2000@vip.163.com

[1] College of Mechanical and Electrical Engineering, Nanjing University of Aeronautics and Astronautics, Nanjing 210016, China

1 Introduction

TiAl intermetallics always possess low density, high specific strength, and specific elastic modulus, superior resistance to oxidation and creep at high-temperature serving environment even above 800 °C [1–3]. Such excellent properties can even allow it to be considered as a candidate for the replacement of nickel-based superalloys, which have been widely used in the intermediate-pressure and high-pressure compressor stators and blades as well as low-pressure turbine blades of turbine aero-engines. A famous application instance of TiAl intermetallics is the employment of a α_2/γ duplex TiAl intermetallic, i.e., Ti-48Al-2Cr-2Nb in the production of the low-pressure turbine blades of GEnx aero-engine [4]. In particular, Ti$_2$AlNb intermetallics, as a newly developed branch and based on an ordered orthorhombic (O($Cmcm$)) phase [5–7], can provide better elongation and specific strength than the conventional TiAl intermetallics (e.g., γ- TiAl) [8, 9], which render such kind of materials a more promising application prospects.

However, it is a well-known fact that titanium alloys are difficult to machine because of the combination of high strength at elevated temperature, low-thermal conductivity, and strong chemical affinity for carbon, nitrogen, oxygen, and halogens, which could facilitate the occurrence of machining thermal damage, excessive tool wear, and poor workpiece surface integrity in the machining process [10–14]. Grinding with conventional (i.e., SiC and Al$_2$O$_3$) and superhard (i.e., CBN and diamond) abrasive wheels is generally used to machine difficult-to-cut materials, e.g., titanium alloys and nickel-based alloys in the aviation manufacturing field [15–24]. In the past two decades, some researches have focused on the grinding process of TiAl intermetallics, most of which involved the evaluation of grindability and surface integrity [4, 25, 26]. For instance, Bentley et al. [25] have characterized the grindability of Ti-48Al-2Cr-2Nb when using SiC
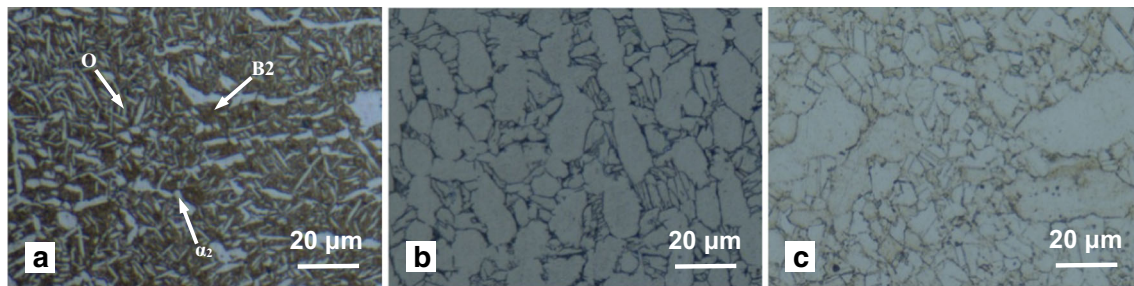
Fig. 1 Metallographical structure for **a** Ti₂AlNb, **b** Ti-6Al-4V, and **c** Inconel718

abrasives and found that, compared to Ti-6Al-4V alloy, a significant increase in G-ratio from 1.5 to 45 and a reduction in surface roughness from 1.4 μm Ra to 0.6 μm Ra could be obtained by using identical operating parameters. Creep feed grinding (CFG) tests on Ti-45Al-8Nb-0.2C have been conducted by Hood et al. [26] using high grit content SiC abrasive wheels, and a G-ratio of ~ 30 could be achieved by using a wheel speed of 15 m/s, workpiece infeed speed of 150 mm/ min and depth of cut of 1.25 mm. The subsequent evaluation of the surface integrity showed a deformation layer of the lamellae with a thickness of ~ 4 μm and a moderate workpiece hardening with a ~ 30% higher hardness over the bulk material. Hood et al. [4] also detailed the performance investigation during CFG of Ti-45Al-2Mn-2Nb + 0.8 vol.% TiB₂ using monolayer electroplated diamond wheels with a wheel speed of 35 m/s and workpiece infeed speed of 150 mm/min. For a grit size of 46 μm and a depth of cut of 0.1 mm, a roughness of Ra = 0.28 μm could be produced after a material removal volume of 3200 mm³ for a wheel width of 20 mm, which stays at an acceptable level in terms of the requirments for a aero-engine component. Moreover, when a grit size of 252 μm was utilized, a considerably higher G-ratio (up to 100) than that during grinding with SiC abrasive could be achieved with a depth of cut of 1 mm. However, though a great progress has been made in understanding the grinding performance of TiAl intermetallics, the grindability characteristics of Ti₂AlNb intermetallics are still unclear.

The objective of this paper is to perform a comprehensive exploration of the grinding characteristics of Ti₂AlNb intermetallics, including grinding force, force ratio, specific grinding energy, G-ratio, surface microstructure and roughness as well as tool wear conditions, with a comparison of Ti-6Al-4V titanium alloy and Inconel718 nickel-based superalloy. In

addition, the reasons for the differences in the grinding characteristics of these three kinds of difficult-to-cut materials are also analyzed.

2 Experimental details

### 2.1 Experimental materials and conditions

The Ti₂AlNb intermetallic used in the present work had a nominal composition of Ti-22Al-25Nb, which showed a triphase structure, i.e., fine-equiaxed α_2-phase, fine-grained B2-phase, and ultrafine-lamellar O-phase, as shown in Fig. 1a. The metallographical structures of Ti-6Al-4V alloy and Inconel718 alloy are also given in Fig. 1b, c, respectively, which showed a significantly larger phase size than Ti₂AlNb. Some important physical/mechanical properties of these three kinds of materials are listed in Table 1. Before grinding, the workpiece materials were cut into 25 mm × 20 mm × 5 mm size via wire cut electrical discharge machining (WEDM), and the grinding experiments were conducted on the 25 mm × 5 mm surface.

The experiments setup is shown in Fig. 2a. All the experiments were carried out in the up-grinding mode on a Blohm Profimat MT-408 surface grinder with a maximum output power of 45 kW and a maximum spindle rotating speed of 8000 r/min. A commercial available green SiC wheel GC80G5V (Fig. 2b) provided by Saint-Gobain Norton Abrasives was employed to grind the workpiece, wherein GC is for green SiC abrasive, 80 is for 160–200 μm grain size, G is for medial wheel rigidity, 5 is for 52% grain volume ratio, and V is for vitrified bond. It was 400 mm in diameter and 20 mm in width. During the grinding experiments for the characterization of grindability and surface integrity, the wheel was dressed by a single-point dimond using wheel speed $v_d = 20$ m/s, infeed rate $f_d = 50$ mm/min, and depth of cut $a_d = 20$ μm with a total dressing depth of 200 μm. In order to yield a fair comparison, the wheel was dressed after each grinding pass. A 5% emulsified liquid with a pressure of 1.5 MPa and a flow quantity of 90 L/min was used to cool the grinding zone. A commonly used wheel speed when grinding difficult-to-cut materials, i.e., $v_s = 20$ m/s [12] was

Table 1 Properties of the workpiece materials at room temperature

Materials	Tensile strength (MPa)	Yield strength (MPa)	Elastic modulus (GPa)	Mirohardness (HV₅₀)	Density (kg/m³)
Ti₂AlNb	1330	1210	130	310	5450
Ti-6Al-4V	950	880	112	305	4390
Inconel718	1420	1250	210	365	8250

Fig. 2 a Experimental setup and **b** surface topography of the wheel used
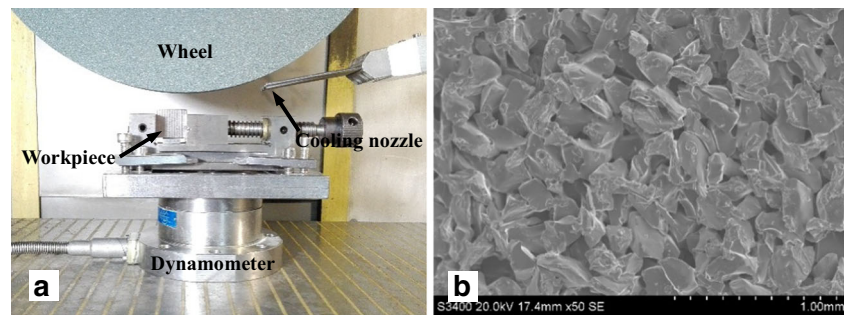
employed while a range of depth of cut a_p (5–20 μm) and workpiece infeed speed v_w (3–12 m/min) were utilized for the variation of grinding parameters. The specified parameters combinations are summarized in Table 2.

2.2 Metrology and measurements

The grinding forces were monitored by a Kistler 9272 piezo-electric dynamometer. After grinding, a sample with a thickness of 2 mm was carefully cut off from the wheel to detect the grinding-induced wheel surface topography. Then a 45 steel razor blade was ground to measure the radial loss of the wheel for the calculation of G-ratio. The ground surface roughness was measured by a Sensofar S neox 3D confocal profilometer, while a Quanta 200 SEM was used to identify the ground surface microstructure. The metallographical structure before and after grinding of the workpiece materials was identified by a Leica DMC 4500 optical microscope. For the metallographical observation, a 3 mm × 3 mm × 4 mm sample was cut off from the ground workpiece via diamond sawing, polished, and then etched using a mixture solution (i.e., HF:HNO$_3$:H$_2$O = 1:3:7 for Ti$_2$AlNb, HF:HNO$_3$:H$_2$O = 1:2:30 for Ti-6Al-4V, and HNO$_3$:H$_2$SO$_4$:HCl = 3:5:92 for Inconel718). During the evaluation of surface integrity, three samples for each grinding conditions were prepared to yield a fair conclusion.

Table 2 Specified grinding parameters combinations used in the current work

Test no.	Grinding speed v_s (m/s)	Depth of cut a_p (μm)	Workpiece infeed speed v_w (m/min)
1	20	10	3
2	20	10	6
3	20	10	9
4	20	10	12
5	20	5	6
6	20	15	6
7	20	20	6

3 Experimental results

3.1 Grinding force, force ratio, and specific grinding energy

Grinding force is one of the most important parameter in grinding process, which affects machined surface roughness, heat flux, residual stress, and surface defects. Figure 3 shows the variation of grinding force as a function of depth of cut and workpiece infeed speed. For the three kinds of workpiece materials, the normal and the tangential grinding forces increased gradually with the increase of the depth of cut and workpiece infeed speed, which could be considered as a result of the increase of undeformed chip thickness. With the same process parameters, the grinding force of Ti$_2$AlNb was about twice larger than those of Ti-6Al-4V, while the normal and the tangential components were only a third and a half of those of Inconel718, respectively.

The grinding force ratio calculated from the force values in Fig. 3 are provided in Fig. 4. For the applied grinding parameters, Ti$_2$AlNb showed a slightly higher average force ratio than Ti-6Al-4V, i.e., 1.58 versus 1.29, which was significantly lower than that of Inconel718 with a value of 2.84.

Specific grinding energy is an important indicator of grindability, which represents the required energy to remove per unit volume of workpiece material. Figure 5 shows the trends of specific grinding energy against depth of cut and workpiece infeed speed. In general, the trends showed a phenomenon known as "size effect" for each workpiece material, revealing the inverse relationship between specific grinding energy and undeformed chip thickness [4]. As the grinding parameters were identical with those in Fig. 3, the quantitative relations between the specific grinding energy of the three workpiece materials were identical with those between the tangential grinding force.
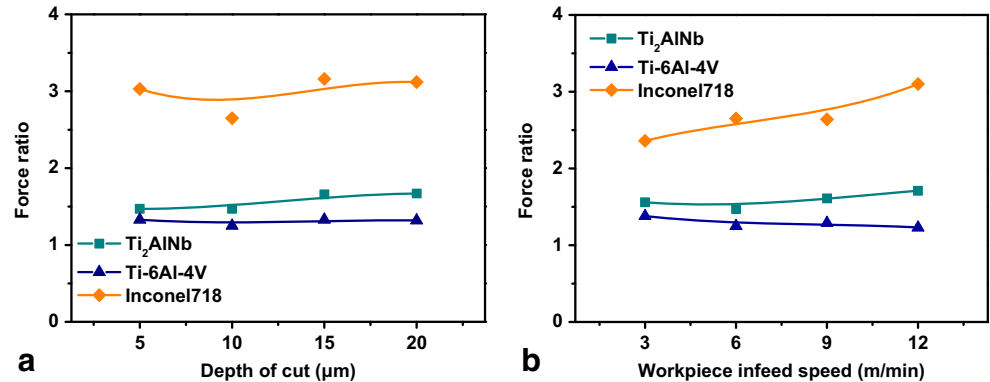
3.2 G-ratio

G-ratio means the wheel wear volume when removing per unit volume of workpiece material, which is another important parameter to characterize the grindability. The G-ratio results for Test 7 are plotted in Fig. 6, which were achieved with a

Fig. 3 Grinding force variation against **a** depth of cut (v_w = 6 m/min) and **b** workpiece infeed speed (a_p = 10 μm)
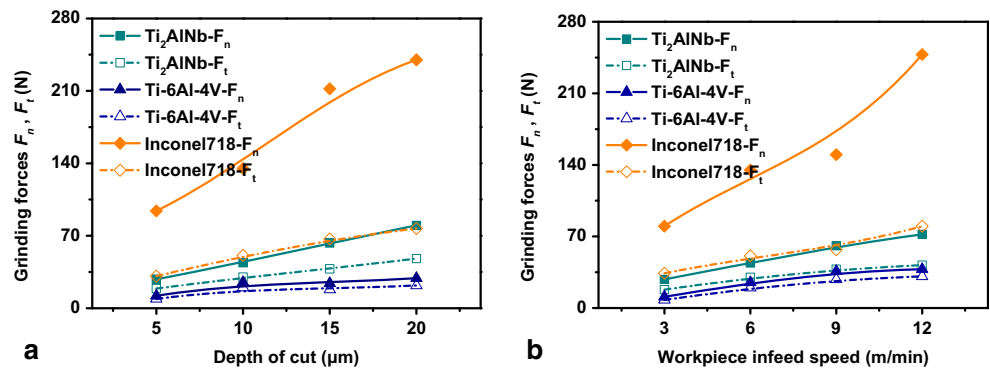
Fig. 4 Force ratio variation against **a** depth of cut (v_w = 6 m/min) and **b** workpiece infeed speed (a_p = 10 μm)

reasonable amount of workpiece material removal, i.e., 100 mm^2 for per unit width of the wheel. It is no surprise that Ti$_2$AlNb exhibited a lower G-ratio value over Ti-6Al-4V, i.e., 0.49 versus 0.73 due to the larger grinding force; however, what is not expected is that the G-ratio of Ti$_2$AlNb was also slightly lower than Inconel718 (0.56), despite the much lower grinding force than the latter. This will be discussed in detail subsequently.

3.3 Surface integrity

3.3.1 Surface microstructure and roughness

Figure 7 shows the SEM observations of the ground surface for Test 1 and Test 7. Except the grinding striations, a natural

attribute of ground surface as a result of cutting behavior of the grain, there were two main microstructure characteristics observed on the ground surface for all the three workpiece materials. One was smeared material formed due to side flow of the workpiece material from the cutting path into the ridges when a grain plowed rather than cut the workpiece. The other was redeposited material which size was generally up to 10 μm. It is interesting to note that more redeposited metal debris is found on the ground surface of Ti$_2$AlNb and Ti-6Al-4V than Inconel718, especially when a higher material removal rate was used.

The microscopic observations of the ground surface for Test 7 have been also identified for the investigation of ground surface roughness, as shown in Fig. 8. The ground surface morphology for all three workpiece materials were mainly

Fig. 5 Specific grinding energy variation against **a** depth of cut (v_w = 6 m/min) and **b** workpiece infeed speed (a_p = 10 μm)
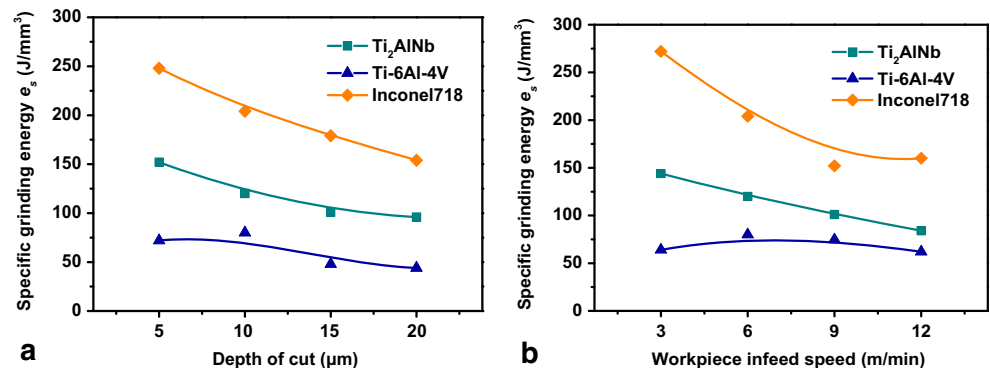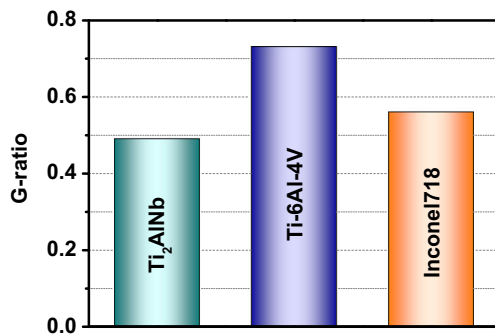
Fig. 6 G-ratio of Ti$_2$AlNb, Ti-6Al-4V, and Inconel718 for Test 7

characterized by relatively regular peak-valley configuration formed due to cutting behavior of the SiC grains. Since the peak-valley distance for all the workpiece materials stayed on a same level, i.e., ~ 2 μm, their surface roughness Ra exhibited a same range, i.e., 0.3–0.6 μm based on an evaluation length of 660 μm (Fig. 8). The surface roughness for Test 1 was also measured; because of space limitation, only surface roughness values were given here, i.e., Ra = 0.35, 0.37, and 0.33 μm for Ti$_2$AlNb, Ti-6Al-4V, and Inconel718, respectively. Such surface roughness results may indicate that the ground surface roughness of Ti$_2$AlNb is more sensitive to the grinding parameters than that of Ti-6Al-4V.

3.3.2 Metallographical alternations

During the grinding process, the workpiece is exposed to excessive thermal and mechanical loadings, which may lead to some metallographical alternations, of which the plastic deformation and the white layer are of particular concern. Figure 9 shows the typical metallographical structure of all three workpiece materials after grinding process for Test 1

and Test 7. Due to the not-very-high material removal rate used, Ti-6Al-4V and Inconel718 showed hardly any metallographical alternations. However, a white layer with a thickness of below 2 μm could be observed on the workpiece subsurface of Ti$_2$AlNb, which evolved from a noncontinuous form (Fig. 9a) into a relatively continuous one (Fig. 9b) when the material removal rate was increased. Such severely deformed workpiece material reveals not only a much higher hardness than the bulk material but also a brittle characteristic [10], which may act as a riser for the fatigue crack during serving time of a ground part. Therefore, for safety concerns, a post-processing technique may be needed to remove the grinding-induced white layer in actual engineering.

3.4 Grinding-induced wheel surface topography

The wheel surface topography after grinding has been also identified to further analyze the grinding mechanisms of Ti$_2$AlNb, as shown in Fig. 10. Some workpiece material adhering to the cutting edges of SiC grains could be observed for all three workpiece materials, primarily revealing a thin-slice pattern. As reported in Ref. [27], during the grinding processes of high-temperature oxidation-resistant metals, including titanium and nickel-based alloys, the uncontaminated material tends to adhere physically to the wheel surface, thereby dulling the wheel. Such adhering behavior of workpiece material will also therefore contribute to the improved power consumption. During the subsequent cutting process, the mechanical loading arising from the cutting behavior of the adhered grain can peel off part of the adhering workpiece material, which can be redeposited to the ground surface (Fig. 7) by the squeezing effect of the grain. Such separation of the adhering workpiece material form the adhered grain could also
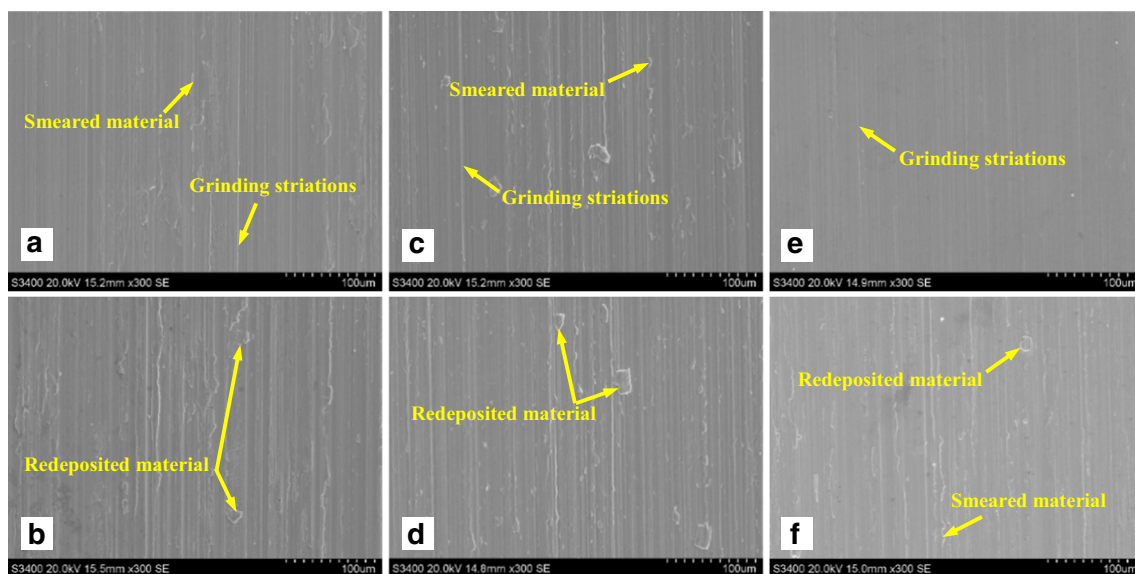
Fig. 7 Ground surface microstructure of **a** Ti$_2$AlNb for Test 1, **b** Ti$_2$AlNb for Test 7, **c** Ti-6Al-4V for Test 1, **d** Ti-6Al-4V for Test 7, **e** Inconel718 for Test 1, and **f** Inconel718 for Test 7
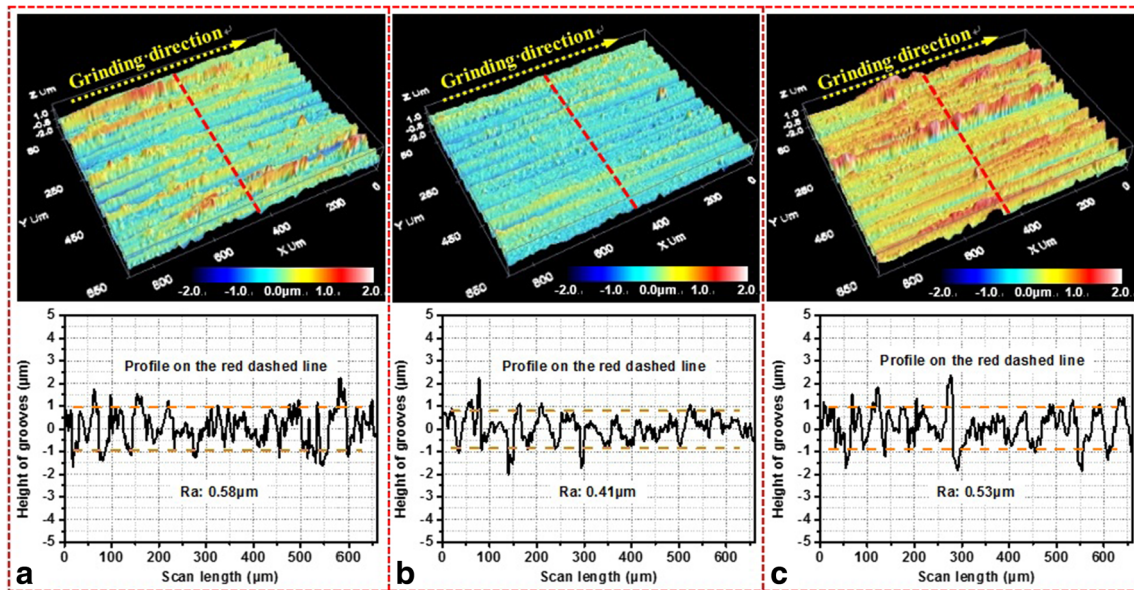
Fig. 8 Ground surface roughness of **a** Ti₂AlNb, **b** Ti-6Al-4V, and **c** Inconel718 for Test 7

render a very few part of the grain material to be chipped off, accelerating the wear rate of the wheel. On the other hand, compared to Inconel718, more adhering workpiece material could be observed on the wheel surface when grinding Ti₂AlNb and Ti-6Al-4V, thereby leading to more redeposited material on the ground surface (Fig. 7).

4 Discussion

As expected, the grinding force of Inconel718 was significantly higher than those of Ti₂AlNb owing to its higher strength and deformation-resistance ability, requiring a greater force

and associated improved power consumption to cut into and remove the workpiece material. However, as stated above, Ti₂AlNb exhibited somehow a slightly lower G-ratio compared to Inconel718. To find out the reasons, the friction coefficient μ between the SiC grains and the workpiece materials, which can quantitatively represent the affinity extent between them has been selected and analyzed.

For a conventional grinding configuration, wherein a shallow depth of cut is utilized, the force conditions of a single grain (Fig. 11a) can be characterized by a chip formation force component F_c, which results from the elastic-plastic deformation of workpiece material, and two frictional force components F_{f1} and F_{f2}, which are required to overcome the friction
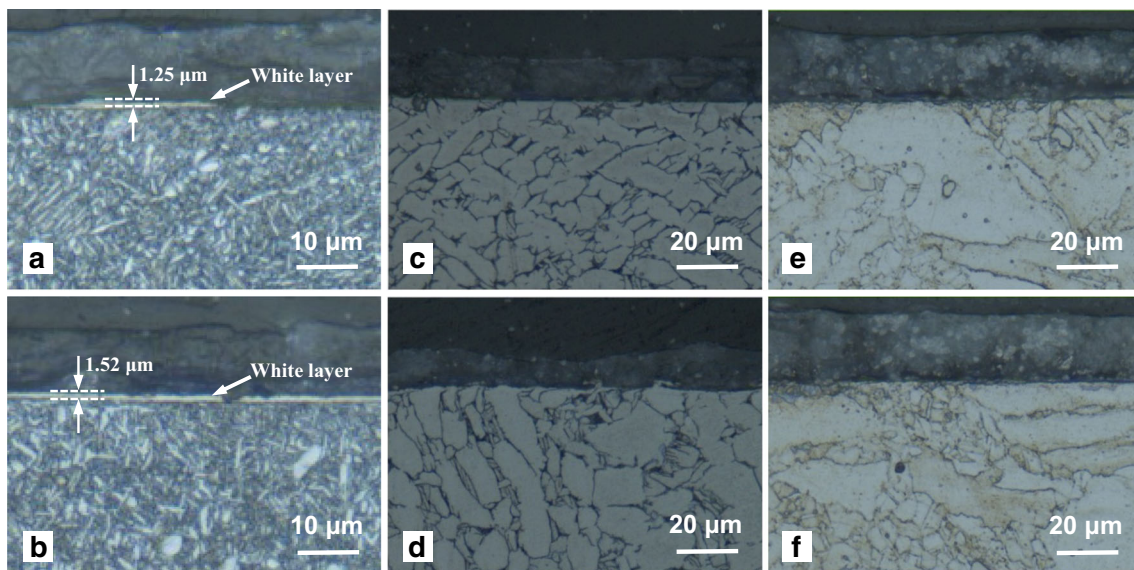
Fig. 9 Metallographical structure of **a** Ti₂AlNb for Test 1, **b** Ti₂AlNb for Test 7, **c** Ti-6Al-4V for Test 1, **d** Ti-6Al-4V for Test 7, **e** Inconel718 for Test 1, and **f** Inconel718 for Test 7
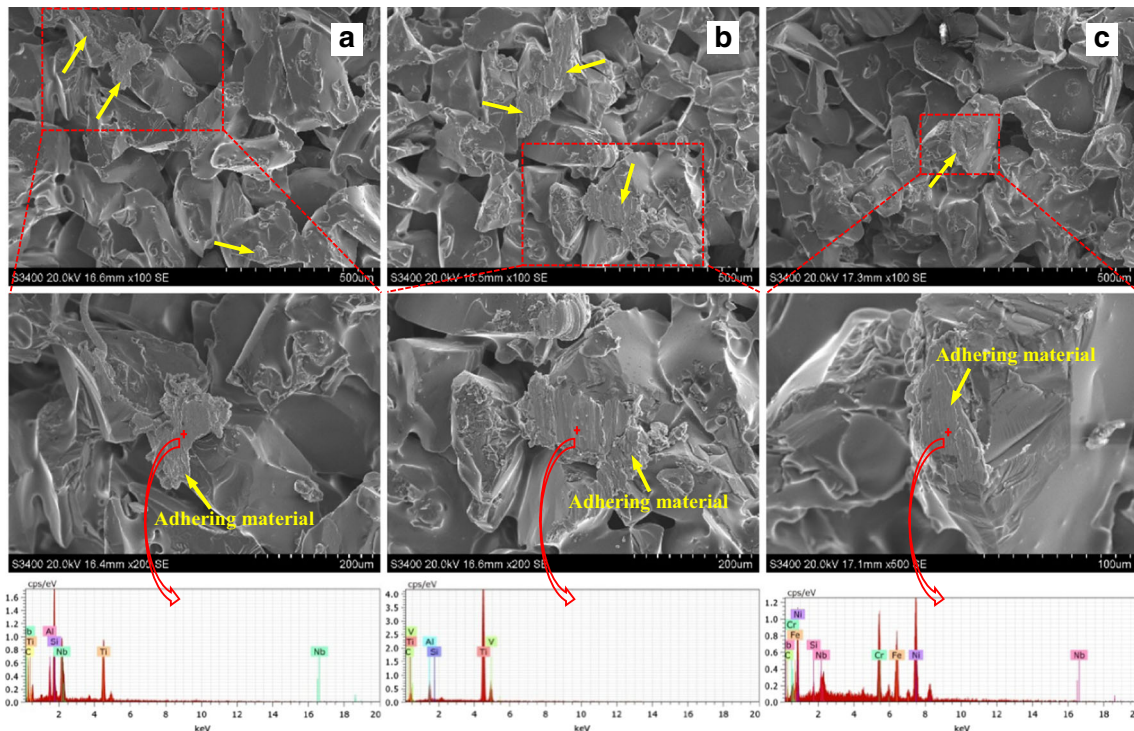
Fig. 10 Wheel surface topography of the after grinding **a** Ti_2AlNb, **b** Ti-6Al-4V, and **c** Inconel718

of the rake and the frank face of the grain with the workpiece, respectively. Based on such analysis, the grinding force components F_t and F_n, measured using a dynamometer, can be divided into the chip formation and the friction segments, as shown in Fig. 11b, such that

$$\begin{cases} F_t = F_{t,c} + F_{t,f} \\ F_n = F_{n,c} + F_{n,f} \end{cases} \tag{1}$$

According to the grinding force model proposed by S. Malkin [28], the frictional force $F_{t,f}$ shows a linear dependence on the contact area A_{con} through a constant pressure p and friction coefficient μ between the wear flat and the workpiece. As such, F_t and F_n could be further expressed as:

$$\begin{cases} F_t = F_{t,c} + \mu \overline{p}_{con} A_{con} \\ F_n = F_{n,c} + \overline{p}_{con} A_{con} \end{cases} \tag{2}$$

By transforming Eq. (2) to remove the effect of the parameter group $\overline{p}_{con} A_{con}$, the mathematical relations among the force components can be given by [28]:

$$F_n = \frac{1}{\mu} F_t + \frac{\mu F_{n,c} - F_{t,c}}{\mu} \tag{3}$$

For the given grinding parameters, $F_{t,c}$ and $F_{n,c}$ are reported to be independent of wheel properties, e.g., wheel sharpness and abrasive options [27, 29]. In the current study, the authors have measured a range of force components F_t and F_n for Test 2, by varying the dressing conditions to generate different wheel sharpness. The applied dressing parameters and the corresponding grinding force responses are summerized in Table 3. Then the F_t and F_n values are re-presented by Fig. 12 to yield the friction efficient, i.e., 0.63, 0.76, and 0.33 for Ti_2AlNb, Ti-6Al-4V, and Inconel718, respectively. This friction coefficient results clearly showed a significantly

Fig. 11 Force condition during grinding process for **a** a single grain and **b** the whole wheel
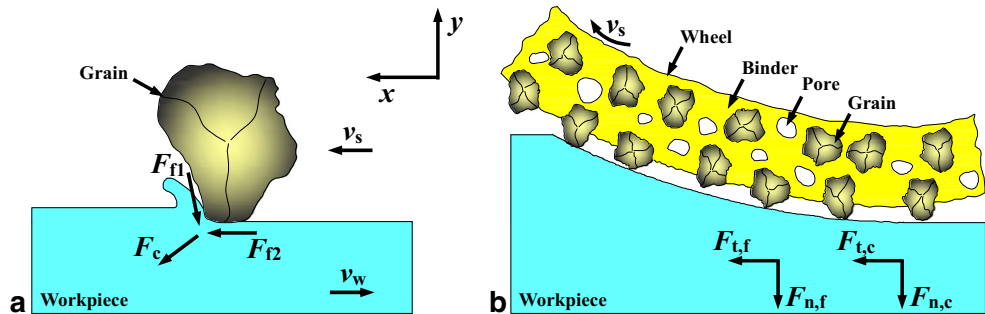
Table 3 Applied dressing parameters and corresponding grinding force responses for calculation of friction coefficient

Dressing parameters			Ti$_2$AlNb		Ti-6Al-4V		Inconel 718	
v_d (m/s)	f_d (mm/min)	a_d (μm)	F_t (N)	F_n (N)	F_t (N)	F_n (N)	F_t (N)	F_n (N)
20	50	5	34.8	56.1	26.1	33.8	62.5	193.3
20	50	10	31.1	49.8	21.5	28.5	57.6	169.5
20	50	15	28.6	45.2	20.8	26.1	47.6	138.4
20	50	20	28.1	45.6	20.2	25.2	46.2	136.6
20	50	25	27.8	44.8	19.1	24.3	45.9	133.1
20	50	30	26.8	43	17.8	23.2	42.6	129.1
20	10	20	34.9	56.3	27.1	34.5	63.1	187.9
20	20	20	31.5	50.2	24.8	32.3	51.2	153.7
20	30	20	30.6	49.2	22.3	28.1	48.3	148.6
20	40	20	31.3	49.2	20.5	27.2	48.1	149.3
20	60	20	31.1	48.6	20.4	26.3	47.6	143.5
20	70	20	30.2	47.8	20.1	26.1	46.6	141.3

higher affinity of Ti$_2$AlNb and Ti-6Al-4V for SiC abrasive in comparison with Inconel718.

An important contributor to such friction coefficient results may be that, apart from the physical adhesion, some particular chemical reactions between the SiC grains and the workpiece materials can occur during the grinding processes of Ti$_2$AlNb and Ti-6Al-4V. Actually, for the SiC grinding of titanium alloys, the dissociation of grain material can commence at elevated temperature by the chemical reaction in Eq. (4) [13]. Such chemical reaction will facilitate a firm bonding between the workpiece and the SiC grains through another chemical reaction shown in Eq. (5), which can significantly improve the adhering effect of the workpiece material to the SiC grains.

$$SiC + O_2 \rightarrow SiO_2 + C \tag{4}$$

$$Ti + C \rightarrow TiC \tag{5}$$

The abovementioned findings imply that, the wheel wear and associated G-ratio results are affected by two factors: (I) mechanical loading acting on the SiC grains, which can result in the routine wear of the wheel, i.e., flattening, fracture, and pullout of the grains and (II) physical and/or chemical bonding between the workpiece and the SiC grains, which can result in

chipping off of the grain material. That is, Ti$_2$AlNb showed a slightly lower G-ratio than Inconel718 because of the relatively strong affinity for the SiC grains, despite much lower grinding force; Ti-6Al-4V showed a higher G-ratio than Inconel718 because of significantly lower grinding force, despite much stronger affinity for the SiC grains. Based on the relationship in Eq. (2), the grinding force ratio can be represented by Eq. (6), indicating that the high friction coefficient between Ti$_2$AlNb/Ti-6Al-4V and the SiC grains owing to the strong affinity in both physical and chemical between them, is one of the main causes of the low grinding force ratio for these two materials.

$$F_n/F_t = \frac{F_{n,c} + \overline{p}_{con} A_{con}}{F_{t,c} + \mu \overline{p}_{con} A_{con}} \tag{6}$$

The findings of the current study suggest to utilize CBN abrasive in grinding of Ti$_2$AlNb, the good wear resistance and chemical stability of which are expected to facilitate a favorable machining performance [30–35], including low grinding force, smooth ground surface, and high G-ratio. An appropriate coolant option is also necessary for the sufficient lubrication of the grinding zone.
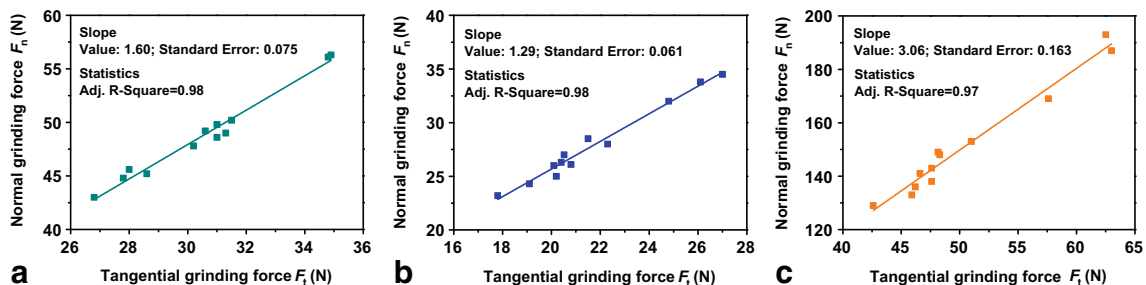
Fig. 12 Fitting of linear relationship between normal and tangential grinding forces listed in Table 3 for **a** Ti$_2$AlNb, **b** Ti-6Al-4V, and **c** Inconel718

5 Conclusions

(1) When using SiC abrasive, Ti$_2$AlNb is harder to grind than Ti-6Al-4V with about twofold force, twofold-specific grinding energy, and 34% lower G-ratio, and is generally easier to grind than Inconel718 with about a half of tangential force and associated a half of specific grinding energy, a third of normal force and slightly lower G-ratio. All three workpiece materials show a same ground surface roughness level, i.e., 0.3–0.6 μm for the applied grinding parameters. In addition, a thin continuous or noncontinuous white layer can easily be formed at the workpiece subsurface when grinding Ti$_2$AlNb, which adversely affects the surface integrity.

(2) During the grinding process with SiC abrasive, Ti$_2$AlNb experiences more excessive tool wear compared to Inconel718 due to strong affinity for the abrasive.

(3) The findings of the current study point to the utilization of CBN superabrasive when grinding Ti$_2$AlNb for a favorable machining performance, including low grinding force, smooth ground surface, and high G-ratio.

References

1. Zhao K, Feng NX, Wang YW (2017) Fabrication of Ti-Al intermetallics by a two-stage aluminothermic reduction process using Na$_2$TiF$_6$. Intermetallics 85:156–162

2. Priarone PC, Rizzuti S, Rotella G, Settineri L (2012) Tool wear and surface quality in milling of a gamma-TiAl intermetallic. Int J Adv Manuf Technol 61:25–33

3. Pflumm R, Friedle S, Schütze M (2015) Oxidation protection of γ-TiAl-based alloys—a review. Intermetallics 56:1–14

4. Hood R, Cooper P, Aspinwall DK, Soo SL, Lee DS (2015) Creep feed grinding of γ-TiAl using single layer electroplated diamond superabrasive wheels. CIRP Ann Manuf Technol 11:36–44

5. Dey SR, Roy S, Suwas S, Fundenberger JJ, Ray RK (2010) Annealing response of the intermetallic alloy Ti-22Al-25Nb. Intermetallics 18:1122–1131

6. Li YJ, Zhao Y, Li Q, Wu AP, Zhu RC, Wang GQ (2017) Effects of welding condition on weld shape and distortion in electron beam welded Ti$_2$AlNb alloy joints. Mater Des 114:226–233

7. Tang F, Nakazawa S, Hagiwara M (2002) The effect of quaternary additions on the microstructures and mechanical properties of orthorhombic Ti$_2$AlNb-based alloys. Mater Sci Eng A 6:492–498

8. Cai DT, Chen JC, Mao XF, Hao CY (2013) Reheat cracking in Ti$_2$AlNb alloy resistance spot weldments. Intermetallics 38:63–69

9. Dey SR, Suwas S, Fundenberger JJ, Ray RK (2009) Evolution of crystallographic texture and microstructure in the orthorhombic phase of a two-phase alloy Ti-22Al-25Nb. Intermetallics 17:622–633

10. Ulutan D, Ozel T (2011) Machining induced surface integrity in titanium and nickel alloys: a review. Int J Mach Tool Manu 51:250–280

11. Aspinwall DK, Dewes RC, Mantle AL (2005) The machining of γ-TiAl intermetallic alloys. CIRP Ann Manuf Technol 54:99–104

12. Klocke F, Soo SL, Karpuschewski B, Webster JA, Novovic D, Elfizy A, Axinte DA, Tönissen S (2015) Abrasive machining of advanced aerospace alloys and composites. CIRP Ann Manuf Technol 64:581–604

13. Xu XP, Yu YQ, Huang H (2003) Mechanisms of abrasive wear in the grinding of titanium (TC4) and nickel (K417) alloys. Wear 255:1421–1426

14. Guo GQ, Liu ZQ, An QL, Chen M (2011) Experimental investigation on conventional grinding of Ti-6Al-4V using SiC abrasive. Int J Adv Manuf Technol 57:135–142

15. Zhang ZY, Guo DM, Kang RK, Gao H, Jin ZJ, Meng YW (2010) Subsurface crystal lattice deformation machined by ultraprecision grinding of soft-brittle CdZnTe crystals. Int J Adv Manuf Technol 47:1065–1081

16. Xi XX, Ding WF, Li Z, Xu JH (2016) High speed grinding of particulate reinforced titanium matrix composites using a monolayer brazed cubic boron nitride wheel. Int J Adv Manuf Technol 90:1529–1538

17. Zhang YB, Li CH, Zhang Q, Jia DZ, Wang S, Zhang DK, Mao C (2016) Improvement of useful flow rate of grinding fluid with simulation schemes. Int J Adv Manuf Technol 84:2113–2126

18. Huang H, Zhang YX, Xu XP (2015) Experimental investigation on the machining characteristics of single-crystal SiC sawing with the fixed diamond wire. Int J Adv Manuf Technol 81:955–965

19. Chandra A, Bastawros AF, Yu TY (2017) Chemical mechanical paired grinding: a tool for multi-wavelength planarization. Int J Adv Manuf Technol 89:611–617

20. Chen ZZ, Xu JH, Ding WF, Ma CY, Fu YC (2015) Grinding temperature during high-efficiency grinding Inconel 718 using porous CBN wheel with multilayer defined grain distribution. Int J Adv Manuf Technol 77:165–172

21. Mao C, Zhou X, Yin LR, Zhang MJ, Tang K, Zhang J (2016) Investigation of the flow field for a double-outlet nozzle during minimum quantity lubrication grinding. Int J Adv Manuf Technol 85:291–298

22. He ZB, Huang H, Yin F, Xu XP (2017) Development of a brazed diamond wire for slicing single-crystal SiC ingots. Int J Adv Manuf Technol 91:189–199

23. Yu TY, Asplund DT, Bastawros AF, Chandra A (2016) Performance and modeling of paired polishing process. Int J Mach Tool Manu 109:49–57

24. Dai CW, Ding WF, Xu JH, Fu YC, Yu TY (2017) Influence of grain wear on material removal behavior during grinding nickel-based superalloy with a single diamond grain. Int J Mach Tool Manu 113:49–58

25. Bentley SA, Aspinwall DK (1997) A comparison of the grinding of IMI318 titanium alloy and a gamma titanium aluminide intermetallic. In: Proceedings of the 32nd International MATADOR Conference, Jul. 10-11; Manchester, p 331-336

26. Hood R, Lechner F, Aspinwall DK, Soo SL, Lee DS (2007) Creep feed grinding of gamma titanium aluminide and burn resistant titanium alloys using SiC abrasive. Int J Mach Tool Manu 47(9):1486–1492

27. Malkin S (1989) Grinding technology: theory and application of machining with abrasives. Wiley, New York

28. Hwang TW, Evans CJ, Malkin S (2000) High speed grinding of silicon nitride with electroplated diamond wheels, part 2: wheel topography and grinding mechanisms. J Manuf Sci Eng 122:42–50

29. Yao CF, Wang T, Xiao W, Huang XC, Ren JX (2014) Experimental study on grinding force and grinding temperature of Aermet 100 steel in surface grinding. J Mater Process Technol 214:2191–2199

30. Mao C, Ren YH, Gan HY, Zhang MJ, Zhang J, Tang K (2015) Microstructure and mechanical properties of cBN-WC-Co composites used for cutting tools. Int J Adv Manuf Technol 76:2043–2049

31. Yu TY, Bastawros AF, Chandra A (2015) Modeling wear process of electroplated CBN grinding wheel. In: Proceedings of the ASME 2015 international manufacturing science and engineering conference, Jun. 8–12; Charlotte, p 1–7

32. Yu TY, Bastawros AF, Chandra A (2014) Experimental characterization of electroplated CBN grinding wheel wear: topology evolution and interfacial toughness. In: Proceedings of the ASME 2014 international manufacturing science and engineering conference, Jun. 9–13; Detroit, p 1–8

33. Yu TY, Bastawros AF, Chandra A (2017) Experimental and modeling characterization of wear and life expectancy of electroplated CBN grinding wheels. Int J Mach Tool Manu 121:70–80

34. Ding WF, Dai CW, Yu TY, Xu JH, Fu YC (2017) Grinding performance of textured monolayer CBN wheels: undeformed chip thickness nonuniformity modeling and ground surface topography prediction. Int J Mach Tool Manu 122:66–80

35. Zhu YJ, Ding WF, Yu TY, Xu JH, Fu YC, Su HH (2017) Investigation on stress distribution and wear behavior of brazed polycrystalline cubic boron nitride superabrasive grains: numerical simulation and experimental study. Wear 376-377:1234–1244